ISSN 1753-3562

2023 Volume 64 Number 1

PHYSICS AND CHEMISTRY OF GLASSES

European Journal of Glass Science and Technology Part B

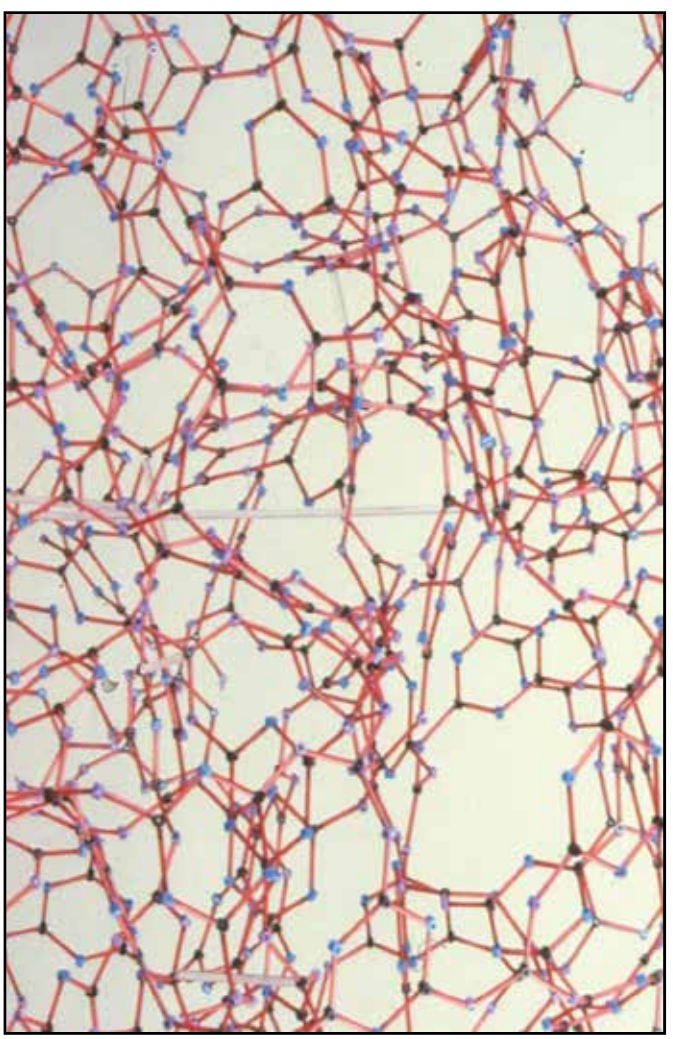

Volume 64 Number 1 **2023**

Physics and Chemistry of Glasses

European Journal of Glass Science and Technology B

CONTENTS

Cover image: Central section of a 3-dimensional random network model of vitreous B_2O_3, with approximately equal numbers of planar (2-dimensional) $B_3O_3Ø_3$ boroxol groups and planar independent $BØ_3$ basic structural units. Borate Networks: Rigidity versus Dimensionality by Adrian C. Wright & Natalia M. Vedishcheva, *Phys. Chem. Glasses: Eur. J. Glass Sci. Technol. B*, February 2016, **57** (1), 1–14.

The European Journal of Glass Science and Technology is a publishing partnership between the Deutsche Glastechnische Gesellschaft and the Society of Glass Technology. Manuscript submissions can be made through Editorial Manager, see the inside back cover for more details.

Society of Glass Technology
9 Churchill Way
Chapeltown
Sheffield S35 2PY, UK
Tel +44(0)114 263 4455
Email info@sgt.org
Web http://www.sgt.org

The Society of Glass Technology is a registered charity no. 237438.

Advertising
Requests for display rates, space orders or editorial can be obtained from the above address.

Physics and Chemistry of Glasses: European Journal of Glass Science and Technology, Part B
ISSN 1753-3562 (Print)
ISSN 1750-6689 (Online)

The journal is published six times a year at the beginning of alternate months from February.

Electronic journals: peer reviewed papers can be viewed by subscribers through Ingenta Select
http://www.ingentaconnect.com

Phys. Chem. Glasses: Eur. J. Glass Sci. Technol. B, 2023, **64** (1), 16–22

Atomistic nature of amorphous graphite

C. Ugwumadu, K. Nepal, R. Thapa & D. A. Drabold†*

Department of Physics and Astronomy, Nanoscale and Quantum Phenomena Institute (NQPI), Ohio University, Athens, Ohio 45701, USA

Manuscript received 27 August 2022
Revised version received 15 November 2022
Accepted 28 November 2022

This paper focuses on the structural, electronic, and vibrational features of amorphous graphite [R. Thapa et al, Phys. Rev. Lett., 2022, **128***, 236402]. The structural order in amorphous graphite is discussed and compared with graphite and amorphous carbon. The electronic density of states and localization in these phases were analyzed. Spatial projection of charge densities in the π bands showed a high charge concentration on participating atoms in connecting hexagons. A vibrational density of states was computed and is potentially an experimentally testable fingerprint of the material. An analysis of the vibrational modes was carried out using the phase quotient, and the mode stretching character. The average thermal conductivity calculated for aG was 0·85 and 0·96 W/cmK at room temperature and 1000 K, respectively.*

I. Introduction

The growing and unmet industrial demand for graphite, coupled with the associated environmental problems resulting from graphite mining activities have become a critical issue.[1] While the graphite feedstock used for only lithium batteries was projected to reach an annual demand of 1·25 million tonnes by 2025,[2] the total amount of mined graphite was only 1 million tonnes in 2021.[3] A promising method intended to mitigate the graphite supply shortage involves a "second-life" approach of graphite recycling/reuse from the spent lithium ion batteries.[4–8] However, recent reports suggest that the environmental and economic implications of industrial-scale second-life graphite are still not favourable.[9–12] Another area of tremendous research interest is the graphitization of naturally occurring carbonaceous materials like coal.[13–18] Beyond the obvious ecological and economic benefits, the actualisation of this form of modern-day alchemy would revolutionise the frontiers of science and engineering. Unfortunately, large-scale graphitization has not yet been achieved and any attempt to realise this would undoubtedly require a synergy between experiments and simulations.

It has been suspected from experiments that graphitization occurs near 3000 K, but until recently, the details of the formation process and nature of the disorder in the planes remained unknown. Our recent prediction of amorphous graphite (aG) from *ab initio* and machine learning molecular dynamic simulations suggested the possibility that the material exists.[19] We showed that carbon has an overwhelming tendency to layer, even with topological defects like 5- and 7-member rings, which fit quite naturally into the network. This discovery has fostered a renewed experimental interest in the path to synthetic forms of graphite from non-crystalline carbon structures. However, a detailed study of the atomistic nature of this carbon structure is required for significant new advances.

In this paper, we elucidate the structural, electronic, and vibrational properties of aG using an ensemble of model sizes ranging from 160–3200 atoms. We investigated the effects of the periodic boundary conditions (PBC) in the formation process of aG and compared the atomic structure of aG to graphite and amorphous carbon. We explored the electronic structure and vibrations by computing the density of states and their corresponding inverse participation ratio. Additionally for the phonon vibrations, the phase quotient, and bond-stretching character were computed. We note here that, except stated otherwise, the analysis herein for the aG was compared with a pristine graphite model (pG) and low-density amorphous carbon (aC) taken from Refs 20 and 21, respectively. Molecular dynamics calculations were done using the "Vienna *Ab initio* Simulation Package" (VASP) with plane-wave potentials,[22] and the "Large-scale Atomic/Molecular Massively Parallel Simulator" (LAMMPS)[23] using the Machine-learning Gaussian Approximation Potential (ML-GAP).[24] Finally, a subscript "*n*" which represents the number of atoms in the system will be used to define the amorphous graphite models (aG_n).

Email * cu884120@ohio.edu, † drabold@ohio.edu
Original version presented at 16th International Conference on the Physics of Non-Crystalline Solids, Canterbury, UK, 10–16 July 2022
DOI: 10.13036/17533562.64.1.18

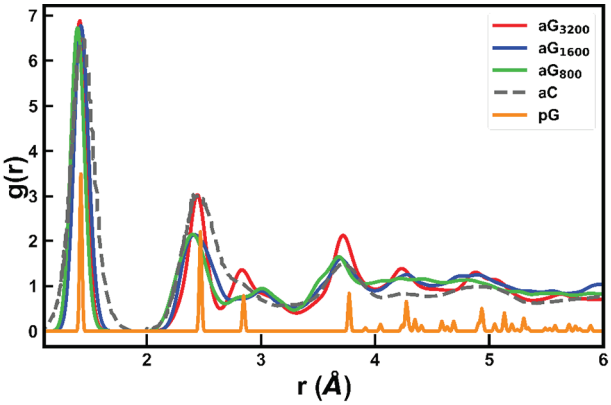

Figure 1. Radial distribution function g(r) for different aG models compared with pG and aC [Colour available online]

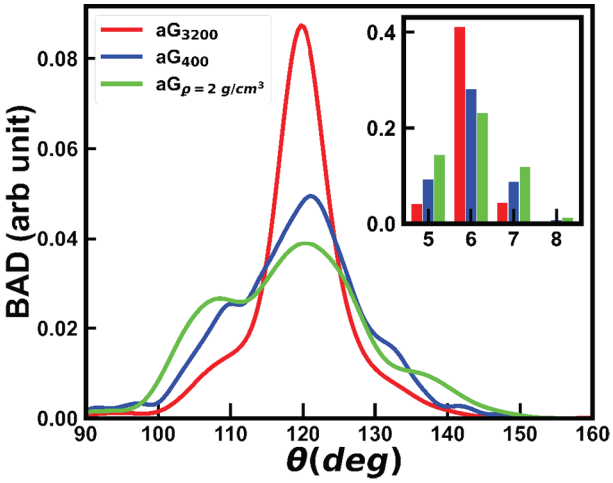

Figure 2. Bond angle distribution (BAD) analysis and ring statistics (inset) for aG_{3200} (red), aG_{400} (blue) and a 160-atom aG model with a density of 2 g/cm^3 (green). The distribution has been smoothed to clearly show the peaks [Colour available online]

II. Formation and structure

A detailed description of the simulation protocol for aG can be found in Ref. 19. In short, the aG formation process involves annealing of *ab initio* models of amorphous carbon or a random starting configuration of carbon atoms within the "formation density" range of ca. 2·2–2·8 g/cm^3 in a canonical (NVT) ensemble at temperatures ranging from 2700–4000 K for up to 500 ps. For this work, we generated an ensemble of structural models (15 models for each aG_n) from different starting configurations at 3000 K and density of 2·44 g/cm^3. The temperature was controlled using the Nosé–Hoover thermostat as implemented within VASP and LAMMPS. The animation for the aG formation process, provided in the supplementary material,[25] indicates that aG is formed in a two-stage process. (1) Conversion of non-sp^2 into sp^2 coordination. (2) The separation of the layers of sp^2 atoms into amorphous graphene sheets.

The formation of aG is also dependent on the periodic boundary condition (PBC) applied. We observed that for aG, the PBC must be applied in three dimensions. In another work, we reported on the formation of buckyonions from a random C network placed in a 3D vacuum, such that periodic boundary condition describes a system of isolated carbon clusters. In the same light, we found nanotubes by maintaining the PBC along the z-axis only (cylindrical symmetry).[26]

The structural order of aG models was analysed using pair correlation functions. Figure 1 compares the peaks obtained for the aG models with pG and aC. The first peak for all aG was within the nearest neighbour C–C bond length observed in graphite. The aG models reproduced more graphitic peaks as the system size increased. This is a consequence of the higher ratio of hexagonal to non-hexagonal rings (6:*n*; *n*=5 or 7) found in large aG systems.

The 6:*n* ring ratio for the models was further confirmed from the bond angle distribution (BAD) and ring statistics. Figure 2 shows the C–C–C angle distribution in aG_{3200} (red), aG_{400} (blue), and aG formed at a lower "threshold" density of 2·0 g/cm^3 (green). We will henceforth refer to the aG formed at 2·0 g/cm^3 as $aG_{<\rho}$. The BAD curve for aG_{3200} (aG_{400}) showed a sharp (flattened) peak at 120°. The broad peak at 109° relates to non-hexagonal rings in the matrix. The ring statistics in the inset of Figure 2 confirmed that aG_{3200} has a higher 6:*n* ring ratio when compared to the other two models. Importantly, Figure 2 (inset) indicates that the ratio of the 5- to 7-member rings (5:7) in aG_{400} and $aG_{<\rho}$ is equal to and greater than unity, respectively. In graphite-like structures with topological defects (i.e aG), planarity is achieved only if the positive curvature induced by a pentagonal ring is compensated by a negative curvature from a neighbouring heptagon (or octagon) ring.[27–29] Deviation from a 1:1 ratio of pentagons and heptagons for an indeterminate number of hexagonal rings results

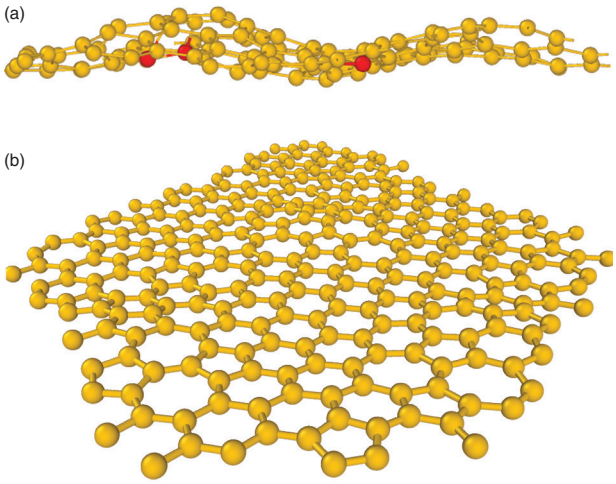

Figure 3. A representative layer for (a) the undulating (worm-like) structure (ρ=2 g/cm^3) and (b) flat structure for aG formed below and within the desired density (ρ=2·44 g/cm^3), respectively. Yellow (red) represents three-fold (four-fold) coordination [Colour available online]

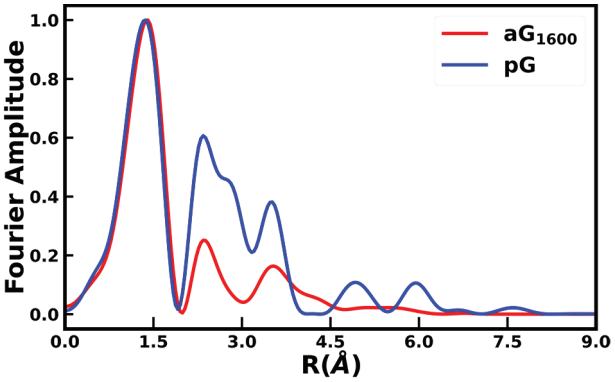

Figure 4. Normalized Fourier amplitude for the C K-edge EXAFS spectra for pG and aG_{1600} [Colour available online]

in a complicated structure like the undulating, "worm-like" layers seen in $aG_{<\rho}$ (see Figure 3(a)), as opposed to "almost" flat layers observed in aG within the desired density (see Figure 3(b)).

Next, we analyzed the local conformation and coordination number (N) of the aG models by implementing an *ab initio* multiple scattering calculations of the extended x-ray absorption fine structure (EXAFS) using the real-space Green's function code FEFF10[30] for the K-edge. Using the Kaiser windowing function, with β=2,[31] the extracted post-edge oscillations ($\chi(E)$) were Fourier transformed (FT) into real space, and the resulting spectrum gives the radial distribution function (RDF). Figure 4 compares the normalized Fourier amplitude acquired for aG_{1600} and pG. All the peaks in aG_{1600} corresponded with some peaks in pG. The first peak at 0·134 nm is due to the first-neighbour C–C scattering (0·142 nm, N=3).[32] The second (0·243 nm, N=6) and third (0·281 nm, N=3) peaks in pG were resolved as a single second peak in aG at 0·243 nm. This "second peak" in aG has been identified in low-density amorphous carbon by Bhattarai and co-workers.[21] Unlike pG, the aG model did not produce additional peaks beyond the fourth C–C scattering peak at 0·38 nm and this suggests an intermediate-range order in aG. We note here that the FT peaks calculated for pG are consistent with those published in literature[32–34] and the results for aG are in agreement with the pair correlation function calculations in Figure 1. This presents a prediction to be employed with experiments.

III. Electronic structure

The electronic density of states (EDoS) for aG was computed within VASP and the extent of localization of Kohn–Sham states (ϕ) was calculated as the electronic inverse participation ratio (EIPR) using the following equation:

$$I(\phi_n) = \frac{\sum_i |a_n^i|^4}{\left(\sum_i |a_n^i|^2\right)^2} \quad (1)$$

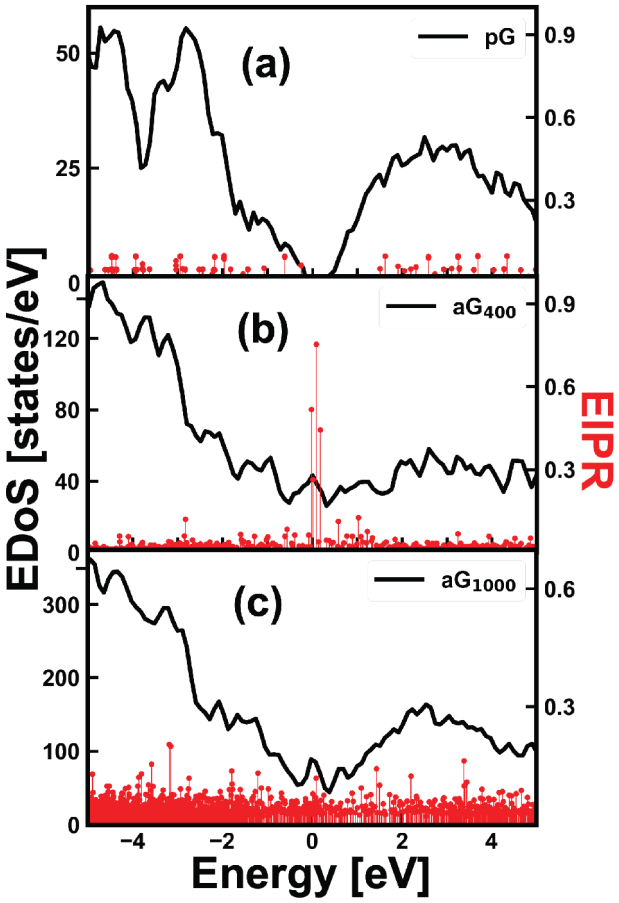

Figure 5. Electronic DoS and IPR for pG and some aG models [Colour available online]

where a_n^i is the contribution to the eigenvector (n) from the i-th atomic orbital. High (low) values of EIPR indicate localised (extended) states.

The EDoS and EIPR for pG, aG_{400} and aG_{1000} are shown in Figure 5(a)–(c) with the Fermi-level (E_f) shifted to zero. Figure 5(a) depicts an expected gap at E_f in pG, with low EIPR values for states in the conduction and valence region.[35] On the other hand, aG does not show any gap at E_f, and some states are localized (see Figure 5(b) and (c). The states with the highest EIPR values were predominantly distributed among non-hexagonal rings in the matrix as shown in Figure 6.

In Ref. 19, using the space-projected conductivity (SPC) formalism,[36] we showed that the conduction-active path in aG was exclusively along connecting atoms in hexagonal rings. To further develop this, we projected the laterally averaged charge density for the π orbitals onto the planes of atoms. Our result, presented as a contour heat-map plot in Figure 7(a), revealed that the regions with the highest values are on the planes with highly connected hexagonal rings (see illustration in Figure 7(b). This is consistent with our initial findings from topological disorder in its layers, to some extent, aG possesses a degree of order in the way the electrons interact in-plane (σ electrons) and out-of-plane (π electrons).

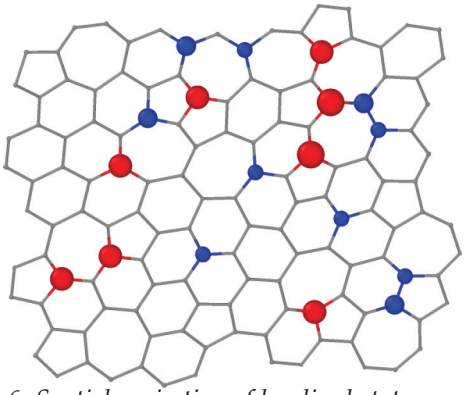

Figure 6. Spatial projection of localized states near E_f on the atoms in aG_{400}. Two states with the highest EIPR in Figure 5(b) are projected as red- and blue-coloured spheres [Colour available online]

IV. Vibrations

Thermal and mechanical properties, as well as the local bonding environment, can be obtained from the vibrations of amorphous materials. The harmonic approximation for vibrations requires evaluating the Hessian matrix, which is accomplished by force calculation from 0·015 Å atomic displacements in six directions (±*x*, ±*y*, ±*z*). The vibrational density of states (VDoS) is calculated as:

$$g(\omega) = \frac{1}{3N}\sum_{i=1}^{3N}\delta(\omega-\omega_i) \tag{2}$$

where, N and ω_i represent the number of atoms and the eigen-frequencies of normal modes, respectively. The delta function (approximated by a Gaussian with a standard deviation equal to 1·5% the maximum frequency) ensures that high-density values were assigned to vibration frequencies that lie close to the normal modes. The extent of localization of each normal mode frequency was calculated through the vibration inverse participation ratio (VIPR), defined as:

$$V(\omega_n) = = \frac{\sum_{i=1}^{N}\left|\mathbf{u}_n^i\right|^4}{\left(\sum_{i=1}^{N}\left|\mathbf{u}_n^i\right|^2\right)^2} \tag{3}$$

where, $\mathbf{u}_n^i$ is the displacement vector of the i-th atom

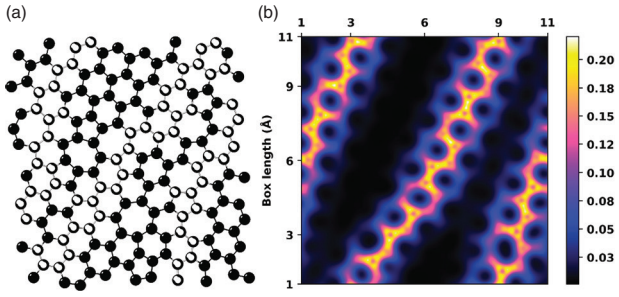

Figure 7. The π orbital charge density distribution projected on a plane of aG. The white-coloured atoms in (a) indicate the connected hexagonal path of the charge density (b) [Colour available online]

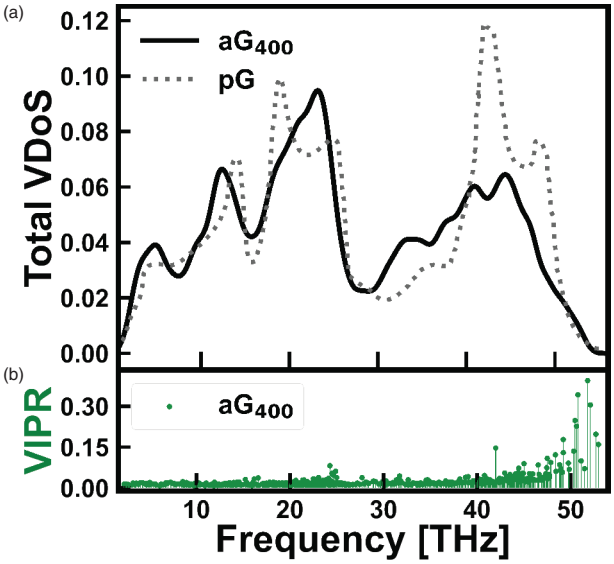

Figure 8. (a) The total VDoS for amorphous and pristine graphite calculated from the harmonic approximation as implemented within VASP. (b) VIPR amorphous graphite. The result is shown for a 400-atom amorphous graphene model [Colour available online]

at normal mode frequency ω_n. By definition, low values of VIPR indicate vibrational mode evenly distributed among the atoms while higher values imply that few atoms contribute at that particular eigen-frequency.

Figure 8(a) shows the total VDoS for amorphous and pristine graphite and Figure 8(b) the extent of localization from the VIPR. While the peaks for aG and pG do not match, the overall shape of both models remained consistent. The figure also provides a vibrational fingerprint of aG to be examined in experiments. The VIPR for aG suggests that more states are localized in the high-frequency region which corresponds to the "optical" mode. The classification of phonon vibrations into pure acoustic and optical modes cannot be rigorously applied for non-crystals due to the lack of periodicity in the lattice, which restricts vibrations to non-propagating modes (e.g. diffusons and locons).[37,38] However, the phase quotient (Q_p) of Bell & Hibbins-Butler[39] provides a measure of how vibrations of neighbouring atoms are in-phase (acoustic mode) and out-of-phase (optical mode). The normalized Q is given as Ref. 40:

$$Q_p = = = \frac{\sum_{i=1}^{N}\left|\mathbf{u}_\mathbf{n}^\mathbf{i}\right|^4}{\left(\sum_{i=1}^{N}\left|\mathbf{u}_\mathbf{n}^\mathbf{i}\right|^2\right)^2} \tag{4}$$

where N_b is the number of valence bonds, $\mathbf{u}_p^i$ and $\mathbf{u}_p^j$ are the normalized displacement vectors (see Equation (3)) for the p-th normal mode. The index, i, sums over all the C atoms and j enumerates neighbouring atoms of the i-th atom. The vibration of the bulk material in unison gives Q_p=1 (purely acoustic). Conversely, a value of −1 would correspond to motion in the opposite direction between neighbouring

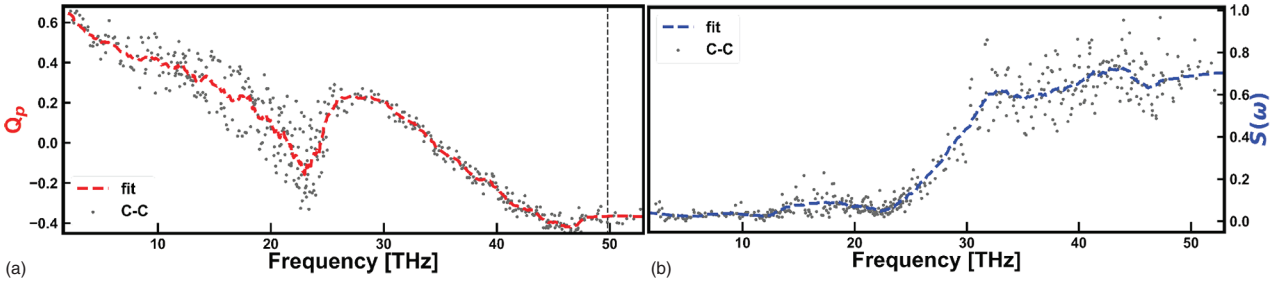

Figure 9. Figure showing (a) the phase quotient and (b) stretching character of aG. The dashed line shows the level at which VIPR=0·15 [Colour available online]

atoms (purely optical). It then follows that positive (negative) Q_p is more "acoustic-like" ("optical- like"). However near 0, one cannot necessarily distinguish between acoustic and optical modes. The phase quotient for aG_{400} is plotted in Figure 9(a). The dashed line identifies the diffuson to locon transition level, which is conceptually the region where VIPR≳0·15.[41] It then follows that the locons have high negative Q_p values at the high-frequency end of the spectrum. Vibrational modes around the inflection point at 23 THz are not locons, but can be considered as quasi-localized "Resonant modes". This results from the finite size of the supercell and diffuses away for larger systems.[42] The animation for vibration at one of the Resonant mode frequencies (see quasiLocalized–freq. mp4 in the supplementary material[25]) confirms that the normal modes are not truly localized but rather majorly distributed amongst C atoms at the boundaries.

We further investigated the vibration modes by calculating the bond-stretching character ($S(\omega)$) of aG using the following equation:

$$S(\omega)=\frac{\sum_m\left|\left(\mathbf{u}_n^i-\mathbf{u}_n^j\right)\right|\hat{\mathbf{r}}_{ij}}{\sum_m\left|\mathbf{u}_n^i-\mathbf{u}_n^j\right|} \tag{5}$$

$\mathbf{u}_n^i$ and $\mathbf{u}_n^j$ are as defined in Equation (3), $\hat{\mathbf{r}}_{ij}$ is the unit vector parallel to the m-th bond. $S(\omega)$ is close to unity when the mode of vibration is predominantly of bond stretching type and will be close to 0 otherwise. The vibrations in aG were observed to be in-plane (out-of-plane) at high (low) frequencies, which are similar to what is found in pristine graphite.[43,44] The in-plane vibrations involve the stretching of C–C bonds of neighbouring atoms, while the out-of-plane vibrations correspond to the breathing mode of individual layers in aG.[45,46] Figure 9 shows that bond stretching in the planes is dominant at high frequencies. We have included two animations in the supplementary material showing the stretching character and breathing mode at the extremes of the frequency spectrum.[25] It is noteworthy that at the mid-spectrum (see quasi-Localized_freq.mp4[25]), there is a combination of both characteristics as predicted from the phase quotient.

We point out that beyond the basic classification of vibrational modes in aG, the optical-like modes (negative Q_p with the bond stretching character) contribute to the thermal conductivity in disordered systems. This has been reported for amorphous carbon in the work of Hamid and coworkers,[47] where they found that at high temperatures (with heat capacity satisfying the Dulong–Petit limit), vibration regions with negative Q_p contribute as much as 40% to the total thermal conductivity. Using LAMMPS, we analyzed the contribution of the topological defect to the thermal conductivity (TC) in aG_{540}. The contribution of the heat flux (**J**) for each atom[48,49] was calculated, and then an ensemble average of the auto-correlation of **J** was related to the TC(κ) using the Green–Kubo formalism given as:[50,51]

$$\kappa=\frac{1}{3VK_BT^2}\int_0^\tau\left\langle\mathbf{J}(0).\mathbf{J}(t)\right\rangle\mathrm{d}t \tag{6}$$

where V, T and K_B are the system volume, temperature, and Boltzmann's constant, respectively. The upper limit of the integral was approximated by τ (=0·5 ns) which is the correlation time required for the heat current autocorrelation to decay to zero. The TC was obtained by averaging the integral in Equation (6) from 15 independent ensembles. The Nosé–Hoover thermostat[52,53] was used for thermalization and equilibration at T=300 and 1000 K in a fixed volume using a 1 fs time-step. At the beginning of the simulation, initial velocities were assigned to the atoms randomly from a Gaussian distribution. Our result showed that the average TC calculated for aG was 0·85 and 0·96 $Wcm^{-1}K^{-1}$ at 300 and 1000 K, respectively. The increase in the thermal conductivity is consistent with what is observed for amorphous systems like aC and amorphous silicon.[47,54,55] We note that the room temperature TC of aG is 5% of that of pyrolytic graphite (κ≈19·5 $Wcm^{-1}K^{-1}$).[55] However, the 11% increase for aG at 1000 K, compared to the 73% decrease for pyrolytic graphite[55] at the same temperature, could be important for applications.

V. Conclusion

This work focused on the structural, electronic and vibration properties of amorphous graphite (aG). aG formed only with PBC in all dimensions within the density range of ca. 2·2–2·8 g/cm^3. However, at a "threshold" density of 2·0 g/cm^3, an undulating

layered structure was observed. Structural features were analyzed and compared to pristine graphite by exploiting the radial distribution function and coordination number. Electronic structure analysis showed that there was no band-gap at the Fermi-level in aG. Few states were observed to be localized on 5- and 7-member rings in the layers. Spatial projection of the charge density near the Fermi-level (π orbitals) showed high values on connecting 6-member rings. The density of state and corresponding participation ratio for the phonon vibrations were analyzed, and the result showed that aG has more states localized at the high-frequency end of the vibration spectrum. Phase quotient and stretching character analysis further suggested that those localized sites were from atoms participating in non-hexagonal rings. The average thermal conductivity for aG was calculated at room temperature (0·85 $Wcm^{-1}K^{-1}$) and 1000 K (0·96 $Wcm^{-1}K^{-1}$) indicated an 11% increase in thermal conductivity.

Acknowledgments

We thank the US Department of Energy for support under Grant No. DE-FE0031981, XSEDE (supported by National Science Foundation Grant No. ACI-1548562) for computational support under allocation no. DMR- 190008P.

The Figures 3 and 6 were made using the Open-Visualization Tool (OVITO).[56] All the animations were made using Jmol.[57]

References

1. Olson, D., Virta, R., Mahdavi, M., Sangine, E. & Fortier, S. Natural graphite demand and supply– implications for electric vehicle battery requirements. In: Geoscience for the Public Good and Global Development: Toward a Sustainable Future, Eds Gregory R. Wessel & Jeffrey K. Greenberg, The Geological Society of America, 2016, **520**, 67.
2. Mills, R. Graphite deficit starting this year, as demand for EV battery anode ingredient exceeds supply. https://www.mining.com/web/graphite-deficit-starting- this-year-as-demand-for-ev-battery-anode-ingredient- exceeds-supply Accessed: 2022-08-03.
3. US Geological Survey, Mineral Commodity Summaries, 2022-Graphite, https://pubs.usgs.gov/periodicals/ mcs2022/mcs2022-graphite.pdf, accessed: 2022-06-25
4. Gao, Y., Wang, C., Zhang, J., Jing, Q., Ma, B., Chen, Y. & Zhang, W. Graphite recycling from the spent lithium-ion batteries by sulfuric acid curing–leaching combined with high-temperature calcination. *ACS Sustainable Chem. Eng*., 2020, **8**, 9447.
5. Liu, D., Qu, X., Zhang, B., Zhao, J., Xie, H. & Yin, H. Alkaline roasting approach to reclaiming lithium and graphite from spent lithium-ion batteries. *ACS Sustainable Chem. Eng*., 2022, **10**, 5739.
6. Bhar, M., Ghosh, S., Krishnamurthy, S., Yalamanchili, K. & Martha, S. K. Electrochemical compatibility of graphite anode from spent Li-ion batteries: Recycled via a greener and sustainable approach. *ACS Sustainable Chem. Eng*., 2022, **10**, 7515.
7. Natarajan, S., Krishnamoorthy, K., Sathyaseelan, A., Mariappan, V. K., Pazhamalai, P., Manoharan, S. & Kim, S.-J. A new route for the recycling of spent lithium-ion batteries towards advanced energy storage, conversion, and harvesting systems. *Nano Energy*, 2022, **101**, 107595.
8. Yi, C., Ge, P., Wu, X., Sun, W. & Yang, Y. Tailoring carbon chains for repairing graphite from spent lithium-ion battery toward closed-circuit recycling. *J. Energy Chem*., 2022, **72**, 97.
9. Velenturf, A. P. & Purnell, P. Principles for a sustainable circular economy. *Sustainable Product. Consumpt.*, 2021, **27**, 1437.
10. Rey, I., Vallejo, C., Santiago, G., Iturrondobeitia, M. & Lizundia, E. Environmental impacts of graphite recycling from spent lithium-ion batteries based on life cycle assessment. *ACS Sustainable Chem. Eng*., 2021, **9**, 14488.
11. Niese, N., Pieper, C., Arora, A. & Xie, A. The Case for a Circular Economy in Electric Vehicle Batteries. https://www.bcg.com/publications/2020/case-for- circular-economy-in-electric-vehicle-batteries Accessed: 2022-08-07
12. Pham, T. T. L. The second life - Challenges of repurposing electric vehicle lithium-ion batteries, The International Institute for Industrial Environmental Economics Master Thesis, 2021.
13. Masi, C. A., Schumacher, T. A., Hilman, J., Dulal, R., Rimal, G., Xu, B., Leonard, B., Tang, J., Fan, M. & Chien, T. Converting raw coal powder into polycrystalline nano-graphite by metal-assisted microwave treatment. *Nano-Struct. Nano-Objects*, 2021, **25**, 100660.
14. Qiu, T., Yang, J.-G. & Bai, X.-J. Preparation of coal-based graphite with different microstructures by adjusting the content of ash and volatile matter in raw coal. *Energy Sources, A: Recovery Utilization Env. Effects*, 2020, **42**, 1874. https://doi.org/10.1080/15567036.2019.1604900
15. Marsh, H. & Rodríguez-Reinoso, F. Production and Reference Material, Chapter 9. In *Activated Carbon*, Eds H. Marsh & F. Rodríguez-Reinoso, Elsevier Science Ltd, Oxford, 2006, pp. 454–508.
16. Qiu, T., Yu, Z., Xie, W., He, Y., Wang, H. & Zhang, T. Preparation of onion-like synthetic graphite with a hierarchical pore structure from anthracite and its electrochemical properties as the anode material of lithium-ion batteries. *Energy Fuels*, 2022, **36**, 8256. https://doi.org/10.1021/acs.energyfuels.2c01892
17. Adamczyk, Z., Komorek, J., Białecka, B., Moszko, J. & Klupa, A. Possibilities of graphitization of unburned carbon from coal fly ash. *Minerals*, 2021, **11**, 1027.
18. Wu, Y., Li, K., Wang, Z., Hu, M., Cao, H. & Liu, Q. Fluctuations in graphitization of coal seam-derived natural graphite upon approaching the Qitianling granite intrusion, Hunan, China. *Minerals*, 2021, **11**, 1147. https://10.3390/min11101147
19. Thapa, R., Ugwumadu, C., Nepal, K., Trembly, J. & Drabold, D. A. Ab initio simulation of amorphous graphite. *Phys. Rev. Lett*., 2022, **128**, 236402.
20. Wyckoff, R. *Crystal Structures, Crystal Structures No. v. 1*, Interscience Publishers, 1963.
21. Bhattarai, B., Biswas, P., Atta-Fynn, R. & Drabold, D. A. Amorphous graphene: a constituent part of low density amorphous carbon. *Phys. Chem. Chem. Phys*., 2018, **20**, 19546.
22. Kresse, G. & Furthmüller, J. Efficient iterative schemes for ab initio total-energy calculations using a plane-wave basis set. *Phys. Rev. B*, 1996, **54**, 11169.
23. Thompson, A. P., Aktulga, H. M., Berger, R., Bolintineanu, D. S., Brown, W. M., Crozier, P. S., in 't Veld, P. J., Kohlmeyer, A., Moore, S. G., Nguyen, T. D., Shan, R., Stevens, M. J., Tranchida, J., Trott, C. & Plimpton, S. J. LAMMPS - a flexible simulation tool for particle-based materials modeling at the atomic, meso, and continuum scales. *Comp. Phys. Commun*., 2022, **271**, 108171.
24. Deringer, V. L. & Csányi, G. Machine learning based interatomic potential for amorphous carbon. *Phys. Rev. B*, 2017, **95**, 094203.
25. Supplemental material describing the animation for the formation of aG and its different phonon vibration modes, which can be found at https://people.ohio.edu/drabold/kent_movies/
26. Ugwumadu, C., Nepal, K., Thapa, R., Lee, Y. G., Majali, Y. A., Trembly, J. & Drabold, D. A. Simulation of multi-shell fullerenes using Machine-Learning Gaussian Approximation Potential. *Carbon Trends*, 2023, **10**, 100239. https://doi.org/10.1016/j.cartre.2022.100239. *See also*: Ugwumadu, C., Thapa, R., Al-Majali, Y., Trembly, J. and Drabold, D.A. Formation of Amorphous Carbon Multi-Walled Nanotubes from Random Initial Configurations. *Phys. Status Solidi B*, 2023, 2200527. https://doi.org/10.1002/pssb.202200527
27. Mackay, A. L. & Terrones, H. Diamond from graphite. *Nature*, 1991, **352**, 762.
28. Terrones, H. & Mackay, A. Hypothetical curved graphite. *Nanostruct. Mater*., 1993, **3**, 319.
29. Lenosky, T., Gonze, X., Teter, M. & Elser, V. Energetics of negatively curved graphitic carbon. *Nature*, 1992, **355**, 333.
30. Kas, J. J., Vila, F. D., Rehr, J. J., Pemmaraju, C. D. & Tan, T. S. Advanced calculations of x-ray spectroscopies with feff10 and corvus. 2021. https://arxiv.org/abs/2106.13334
31. Kaiser, J. F. Digital Filters - Chapter 7. In *Systems analysis by digital computer*, John Wiley and Sons, New York, 1966, pp. 218–285.

32. Comelli, G., Stöhr, J., Jark, W. & Pate, B. B. Extended x-ray-absorption fine-structure studies of diamond and graphite. *Phys. Rev. B*, 1988, **37**, 4383.
33. Tanaka, T., Matsubayashi, N., Imamura, M. & Shimada, H. Synchronous scanning of undulator gap and monochromator for XAFS measurement in soft X-ray region. *J. Synch. Radiat*., 2001, **8**, 345.
34. Buades, B., Moonshiram, D., Sidiropoulos, T. P. H., Léon, I., Schmidt, P., Pi, I., Palo, N. D., Cousin, S. L., Picón, A., Koppens, F. & Biegert, J. Dispersive soft x-ray absorption fine-structure spectroscopy in graphite with an attosecond pulse. *Optica*, 2018, **5**, 502.
35. Drabold, D. A., Ordejón, P., Dong, J. & Martin, R. M. Spectral properties of large fullerenes: From cluster to crystal. *Solid State Commun.*, 1995, **96**, 833.
36. Prasai, K., Subedi, K. N., Ferris, K., Biswas, P. & Drabold, D. A. Spatial Projection of Electronic Conductivity: The Example of Conducting Bridge Memory Materials. *phys. stat. solidi – Rapid Res. Lett*., 2018, **12**, 1800238.
37. Allen, P. B. & Feldman, J. L. Thermal conductivity of disordered harmonic solids. *Phys. Rev. B*, 1993, **48**, 12581.
38. Allen, P. B., Feldman, J. L., Fabian, J. & Wooten, F. Diffusons, locons and propagons: Character of atomic vibrations in amorphous Si. *Philos. Mag. B*, 1999, **79**, 1715.
39. Bell, R. J. & Hibbins-Butler, D. C. Acoustic and optical modes in vitreous silica, germania and beryllium fluoride. *J. Phys. C: Solid State Phys*., 1975, **8**, 787.
40. Bhattarai B. & Drabold, D. A. Amorphous carbon at low densities: An ab initio study. *Carbon*, 2017, **115**, 532–538.
41. Seyf, H. R., Yates, L., Bougher, T. L., Graham, S., Baratunde, T. D., Cola, A., Ji, M.-H., Kim, J., Dupuis, R., Lv, W. & Henry, A. Rethinking phonons: The issue of disorder. *Comput. Mater*., 2017, **3**, 49.
42. Feldman, J. L., Allen, P. B. & Bickham, S. R. Numerical study of low-frequency vibrations in amorphous silicon. *Phys. Rev. B*, 1999, **59**, 3551.
43. Gurney, R. W. Lattice vibrations in graphite. *Phys. Rev*., 1952, **88**, 465.
44. Sherry, P. B. & Coulson, C. A. The vibrational frequency distribution of graphite: I. Out-of-plane modes of a single layer. *Proc. Phys. Soc. B*, 1956, **69**, 1326.
45. Newell, G. F. Vibration spectrum of graphite and boron nitride. ii. The three-dimensional spectrum. *J. Chem. Phys*., 1957, **27**, 240. https://doi.org/10.1063/1.1743680
46. Lui, C. H., Malard, L. M., Kim, S., Lantz, G., Laverge, F. E., Saito, R. & Heinz, T. F. Observation of layer-breathing mode vibrations in few-layer graphene through combination Raman scattering. *Nano Lett*., 2012, **12**, 5539, pMID: 22963681. https://doi.org/10.1021/nl302450s
47. Seyf, H. R., Lv, W., Rohskopf, A. & Henry, A. The importance of phonons with negative phase quotient in disordered solids. *Sci. Rep*., 2018, **8**, 2627.
48. Surblys, D., Matsubara, H., Kikugawa, G. & Ohara, T. Methodology and meaning of computing heat flux via atomic stress in systems with constraint dynamics. *J. Appl. Phys*., 2021, **130**, 215104. https://doi.org/10.1063/5.0070930
49. Surblys, D., Matsubara, H., Kikugawa, G. & Ohara, T. Application of atomic stress to compute heat flux via molecular dynamics for systems with many-body interactions. *Phys. Rev. E*, 2019, **99**, 051301.
50. Green, M. S. Markoff random processes and the statistical mechanics of time-dependent phenomena. ii. Irreversible processes in fluids. *J. Chem. Phys*., 1954, **22**, 398. https://doi.org/10.1063/1.1740082
51. Kubo, R., Yokota, M. & Nakajima, S. Statistical- mechanical theory of irreversible processes. ii. Response to thermal disturbance. *J. Phys. Soc. Jpn*., 1957, **12**, 1203. https://doi.org/10.1143/JPSJ.12.1203
52. Nosé, S. A molecular dynamics method for simulations in the canonical ensemble. *Molec. Phys*., 1984, **52**, 255. https://doi.org/10.1080/00268978400101201
53. Hoover, W. G. Canonical dynamics: Equilibrium phase- space distributions. *Phys. Rev. A*, 1985, **31**, 1695.
54. Allen, P. B. & Feldman, J. L. Thermal conductivity of glasses: Theory and application to amorphous Si. *Phys. Rev. Lett*., 1989, **62**, 645.
55. Ho, C. Y., Powell, R. W. & Liley, P. E. Thermal conductivity of the elements. *J. Phys. Chem. Ref. Data*, 1972, **1**, 279. https://doi.org/10.1063/1.3253100
56. Stukowski, A. Visualization and analysis of atomistic simulation data with OVITO–the open visualization tool. *Model. Simulat. Mater. Sci. Eng*., 2009, **18**, 015012.
57. Jmol: an open-source Java viewer for chemical structures in 3D.